Designing a High-Sensitivity Microscale Triple-Band Biosensor Based on Terahertz MTMs to Provide a Perfect Absorber for Non-Melanoma Skin Cancer Diagnostic

Musa N. Hamza, Mohammad Tariqul Islam, *Senior Member, IEEE*, Slawomir Koziel, *Fellow, IEEE*, Muhamad A. Hamad, Iftikhar ud Din, Ali Farmani, Sunil Lavadiya, and Mohammad Alibakhshikenari

***Abstract*—Non-melanoma skin cancer (NMSC) is among the most prevalent forms of cancer originating in the top layer of the skin, with basal cell carcinoma (BCC) and squamous cell carcinoma (SCC) being its primary categories. While both types are highly treatable, the success of treatment hinges on early diagnosis. Early-stage NMSC detection can be achieved through clinical examination, typically involving visual inspection. An alternative, albeit invasive, method is a skin biopsy. Microwave imaging has gained prominence for non-invasive early detection of various cancers, leveraging distinct dielectric properties of healthy and malignant tissues to discriminate tumors and categorize them as benign or malignant. Recent studies demonstrate the potential of terahertz (THz) spectroscopy for detecting biomarkers by aligning electromagnetic wave frequencies in the low THz range (0.1 to 10 THz) with resonant frequencies of biomolecules, such as proteins. This study proposes an innovative microscale biosensor designed to operate in the THz range for the high-sensitivity and efficient diagnosis of non-melanoma skin cancer. By incorporating meticulously designed metamaterial layers, the sensor's absorption properties can be controlled, a critical aspect for discriminating between normal and NMSC-affected skin. In particular, the interaction between skin and THz waves, influenced by dielectric properties and unique vibrational resonances of molecules within tissue, is crucial for wave propagation and scattering. Extensive numerical studies showcased the suitability of the proposed biosensor for NMSC diagnosis, illustrated through specific case studies. These findings hold the potential to pave the way for further development of non-invasive microwave-imaging-based techniques for detecting NMSC and other types of skin cancer.**

***Index Terms*—Non-melanoma skin cancer (NMSC), cancer diagnosis, microwave imaging, terahertz (THz) spectroscopy, tumor detection, microwave sensors, metamaterials.**

Manuscript received 29 January 2024; revised 5 March 2024; accepted 20 March 2024. Date of publication 27 March 2024; date of current version 10 April 2024. This work was supported in part by the Ministry of Higher Education (MOHE), Malaysia through the Fundamental Research Grant Schemes (FRGS) under Grant FRGS/1/2021/TK0/UKM/01/6, in part by Icelandic Research Fund Grant 239858, and in part by the National Science Centre of Poland under Grant 2020/37/B/ST7/01448. *(Corresponding author: Mohammad Tariqul Islam.)*

Musa N. Hamza is with the Department of Physics, College of Science, University of Raparin, Sulaymaniyah 46012, Iraq (e-mail: musa.nuraden@uor.edu.krd).

Mohammad Tariqul Islam is with the Department of Electrical, Electronic and Systems Engineering, Faculty of Engineering and Built Environment, Universiti Kebangsaan Malaysia, Bangi, Selangor 43600, Malaysia (e-mail: tariqul@ukm.edu.my).

Slawomir Koziel is with the Engineering Optimization & Modeling Center, Reykjavik University, 102 Reykjavik, Iceland, and also with the Faculty of Electronics, Telecommunications and Informatics, Gdansk University of Technology, 80-233 Gdansk, Poland (e-mail: koziel@ru.is).

Muhamad A. Hamad is with the Physics Department, College of Education, Salahaddin University, Erbil 44002, Iraq (e-mail: muhamad.hamad@su.edu.krd).

Iftikhar ud Din is with the Telecommunication Engineering Department, University of Engineering and Technology, Mardan 23200, Pakistan (e-mail: iftikharuddin114@gmail.com).

Ali Farmani is with the Department of Electronics Engineering, Lorestan University, Khorramabad 68151-44316, Iran (e-mail: farmani.a@lu.ac.ir).

Sunil Lavadiya is with the Department of Information and Communication Technology, Marwadi University, Rajkot, Gujarat 360003, India (e-mail: sunil.lavadiya@marwadieducation.edu.in).

Mohammad Alibakhshikenari is with the Department of Signal Theory and Communications, Universidad Carlos III de Madrid, 28911 Leganés, Spain (e-mail: mohammad.alibakhshikenari@uc3m.es).

Digital Object Identifier 10.1109/JPHOT.2024.3381649

I. Introduction

NON-MELANOMA skin cancers (NMSCs) are the most common types of human malignancies, and their incidence is steadily increasing. NMSC includes various skin cancers, with basal cell carcinoma (BCC) and squamous cell carcinoma (SCC) being the most common, making up about 99% of cases. Other types, like Merkel cell carcinoma, sebaceous carcinoma, and apocrine adenocarcinoma, are rarer [1]. BCC is more prevalent, with a ratio to SCC ranging from 1:1 to 10:1, depending on factors like population and ethnicity. Despite NMSC being much more common than cutaneous melanoma, there's not a lot of data on these specific types of tumors [2]. In many European countries, national cancer registries don't distinguish between different NMSC types. Tumor diagnoses follow the International Classification of Diseases 11th Revision (ICD-11). While cutaneous melanoma has a reliable code (C43), the broader NMSC category is coded as C44, making it challenging to get separate data on BCCs, SCCs, and other skin cancers [1].

According to recent statistics, there are around 5.4 million cases of basal cell carcinoma and squamous cell carcinoma reported each year [3]. Superficial BCCs are usually on the trunk, while the more common nodular type is often on the head and neck due to more exposure to intermittent sunlight. Both intermittent and intense sun exposure are the main risk factors for BCC [4]. NMSC, in general, is treatable, and BCC

has a low risk of spreading, estimated between 0.00281% and 0.5% [5]. BCC's mortality rate is exceptionally low, but SCC has a higher risk of spreading, ranging from 0.5% to 16%, with a higher mortality rate [6].

The diagnosis of NMSC in typical cases can be done through clinical examination. SCC usually shows up as rapidly growing pink or red nodules that might be rough or ulcerated. The appearance of BCC depends on the subtype. The most common type, nodular BCC, looks like pink nodules with rolled edges, visible blood vessels, and sometimes ulcers. Superficial BCCs, making up about 20% of cases, are often on the trunk and look like pink scaly patches that might be confused with other skin conditions. Other types, like morphoeic BCC, can look like subtle scar-like patches, and pigmented BCC, more common in Far East populations, might be mistaken for a type of melanoma [7]. Dermoscopy, a tool used for BCC diagnosis, shows specific features like leaf-like areas, blue-grey spots, wheel-spoke patterns, and branching blood vessels. Skin biopsy, aside from confirming the diagnosis, helps categorize tumors as high- or low-risk [8].

The term "metamaterial" is rooted in the Greek language, signifying superiority or beyond. It denotes an artificial synthetic composite material created by amalgamating various elements, including plastic and metals. As per the European Union's definition, metamaterials are described as "an arrangement of man-made structural components designed to achieve advantageous and unusual electromagnetic characteristics" [9]. Metamaterials find widespread use in enhancing antenna system performance, modifying electromagnetic characteristics, absorbing electromagnetic radiation, and altering the elastic properties of materials. Moreover, applications span diverse sectors, encompassing public safety, high-frequency battlefield communications, remote aerospace applications, sensor identification, and military research for detecting explosives and contamination [10], [11], [12], [13], [14], [15]. Presently, researchers are actively exploring the potential of metamaterials across different domains. The electromagnetic characteristics of optical elements, including both fundamental elements and novel metamaterial structures, are determined by two key factors: materials and structures [16]. For bulk materials, properties hinge on the effects of permittivity (ε) and permeability (μ), characterizing the polarizing capability of the material under the influence of electric and magnetic fields, respectively [17]. Metamaterials have introduced innovative avenues for controlling electromagnetic waves, yielding remarkable optical phenomena like superlensing, electromagnetically-induced transparency, perfect absorption, and polarization conversion [18]. As specific subtypes, metamaterials can be manipulated to construct absorbers and polarization converters in the terahertz frequency region, achieving near unity absorption and polarization conversion across a small or broad frequency range. These metamaterial-based terahertz devices can overcome the thickness limitation associated with traditional quarter-wavelength devices [19].

Hongsen Zhang et al. present a novel all-metal nanostructure for a Plasmonic perfect absorber (PPA), exhibiting high absorbance rates across multiple frequencies and potential as a refractive index sensor [20].

Zezhao Ju et al. introduce a method for generating Airy beams using dielectric metasurfaces, offering wide bandwidth operation and remarkable properties such as diffraction-free behavior [21].

A biosensor is a device or probe that integrates a biological element, such as an enzyme or antibody, with an electronic component to generate a measurable signal. The electronic component detects, records, and transmits information concerning physiological changes or the presence of various chemical or biological materials in the environment. Biosensors, available in diverse sizes and shapes, can detect and measure even low concentrations of specific pathogens, toxic chemicals, and pH levels [22]. Shuangyan Gao et al. present a D-type double open-loop channel surface plasmon resonance (SPR) photonic crystal fiber (PCF) for temperature sensing, offering high sensitivity and potential applications across various fields [23].

Recently, THz spectroscopy technology, based on metamaterials, has emerged as a promising biomarker detection method [24]. Yongzhi Cheng et al. propose a straightforward design for a six-band terahertz perfect metasurface absorber (PMSA), showcasing high absorbance across distinct frequencies [25]. Zhaorui Huang et al. suggest an interleaved metalens configuration for high-resolution polarization imaging [26].

The THz wave's frequency range (0.1 THz to 10 THz) aligns with the vibrational frequencies of essential biomolecules, such as proteins, RNA, and DNA, enabling the detection of molecular vibrations. Additionally, THz spectroscopy technology boasts merits like label-free, non-contact, and non-destructive inspection of target biomolecules. These advantages underscore its suitability for biomolecule detection. Concurrently, advancements in micro-nanofabrication technology have facilitated the design of novel THz metamaterials, exhibiting a tailored electromagnetic response. These metamaterials prove highly sensitive to changes in the micro-environment medium on their surface [27]. Chenguang Rong et al. introduce a dual-band terahertz chiral metasurface absorber (CMA) with enhanced circular dichroism (CD) effect, suitable for diverse sensing applications [28]. Another research presents a dual-band terahertz perfect absorber (PA) with high absorbance rates and versatile sensing capabilities [29].

The study goal is to create a novel microscale biosensor by applying terahertz metamaterials with triboelectric technologies. The main goal is to develop a sensitive and effective diagnostic instrument that is especially designed for the identification of skin cancer that is not melanoma. By developing a high-performance biosensor with flawless absorption in the terahertz band, the project hopes to contribute to the precise and timely diagnosis of skin cancer that is not melanoma. In order to improve healthcare outcomes, this entails integrating terahertz metamaterials, triboelectric materials, and microscale technology to improve the sensor's sensitivity, selectivity, and overall diagnostic accuracy.

II. Model's Unit Cell Layout

Fig. 1 shows a 2-D schematic of the recommended structure of the perfect absorber as biosensor, which is composed of model 6,

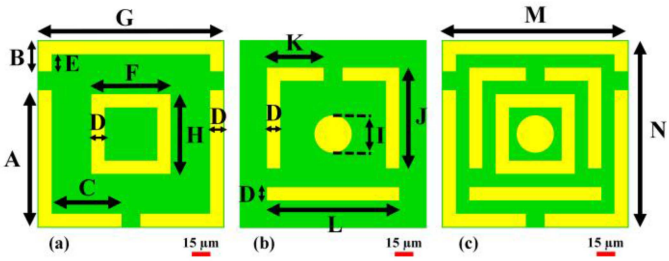

Fig. 1. Recommended structural design for a perfect absorber; (a) model 6, (b) model 9, and (c) model 12 (proposed biosensor design).

TABLE I
COMPLETE LIST OF THE VARIABLES THAT HAVE BEEN ADJUSTED FOR THE RECOMMENDED SENSOR

Parameter	Value (μm)	Parameter	Value (μm)
A	109.25	J	80.5
B	24.25	K	45.5
C	56.14	L	106.1
D	10.6	M	150
E	13.64	N	150
F	63.64	PET thick (T_1)	10
G	148.5	Coverslip thick (T_2)	4
H	63.64	Basal Cells thick (T_3)	4
I	30	Aluminum (Al) thick	0.2

model 9 and model 12. The width parameter G is the side length of the structure and the terahertz interaction length between the resonance part and the square cavity. M and N are the width of the model 12 waveguide. F and H are the coupling distance between the boundary of the square cavity and the waveguide of model 6. D refers to the thickness of metal layer. The refractive index of materials extracted from numerical package. In Table I, all structural parameters is provided which can lead to the appropriate result and perfect absorption is accessible.

The schematic illustrates a 2-D representation of the proposed structure intended to function as a perfect absorber biosensor, comprised of models 6, 9, and 12. The designation of "perfect absorber" is attributed to the meticulous engineering of metamaterial layers within the biosensor, enabling precise control over absorption properties. To compute the configuration parameters of models 6, 9, and 12 at the considered terahertz (THz) frequency, rigorous numerical simulations utilizing finite-difference time-domain (FDTD) methods were employed, allowing for detailed characterization of electromagnetic wave behavior within the biosensor structure, considering factors such as dielectric properties and resonant frequencies of biomolecules within tissue. The resulting parameters are finely tuned to optimize the biosensor's performance in the THz range, ensuring heightened sensitivity and efficiency in NMSC diagnosis. The article also presents twelve distinct models, each possessing unique characteristics suitable for diverse applications, offering potential utility for researchers across various fields. However, in biosensing, where exceptionally high sensitivity is crucial, Model 12 is recommended due to its triple-band configuration, which enhances sensitivity, particularly in discerning nuanced biological signals. This recommendation acknowledges the paramount importance of heightened sensitivity in biosensing applications and aims to propose novel designs, such as the fusion of Designs 6 and 9, yielding a new hybrid model contributing to biosensing technology advancement.

Here, the finite-difference time-domain method (FDTD) as a numerical technique is used to solve electromagnetic field equations in time-domain. It is commonly employed in areas such as optics, photonics, and electromagnetic compatibility studies. By dividing space into a grid of discrete points, and time into equally spaced intervals, FDTD approximates the behavior of electromagnetic fields. In FDTD, Maxwell's equations are discretized and solved iteratively over each point in the grid. By updating the field values at each time step, the method accurately simulates the propagation and interaction of electromagnetic fields in the given space. It can handle a wide range of materials, geometries, and sources, making it a versatile approach for solving electromagnetic field problems. FDTD has numerous applications, including modeling waveguides, antennas, scattering and diffraction phenomena, and analyzing the behavior of photonic structures, among others. Its ability to capture both spatial and temporal characteristics of fields makes it a valuable tool in electromagnetic simulations.

Here, Maxwell's equations are applied to numerical calculation of the proposed structure (1), (2):

$$\frac{\partial E}{\partial t} = \frac{1}{\varepsilon_n} \nabla \times H \tag{1}$$

$$\frac{\partial H}{\partial t} = -\frac{1}{\mu_n} \nabla \times E \tag{2}$$

The optical absorption coefficient (α) is a measure of how strongly a material absorbs light at a given wavelength. It can be calculated using the following formula:

$$\alpha = \left(\frac{1}{d}\right) \ln\left(\frac{1}{T}\right) \tag{3}$$

where:

- α is the optical absorption coefficient in inverse meters (m^{-1})
- d is the thickness of the material in meters (m)
- ln stands for the natural logarithm
- T is the transmittance of light through the material, expressed as a decimal fraction (ranging from 0 to 1)

Achieving precise simulations of micron-scale terahertz (THz) metamaterial absorbers using CST Studio necessitates careful considerations regarding conditioning boundaries and wave sources. Employing absorbing boundary layers, notably Perfectly Matched Layers (PMLs), is vital to prevent undesired reflections and confine energy within the simulation domain, crucial for accurate THz simulations. Ensuring accurate simulation conditions involves employing a domain size significantly larger than the metamaterial structure to minimize near-field interactions with the boundary layers and ensure precise absorption calculations. Meshing strategies require a fine mesh around the metamaterial structure, particularly near sharp features, for an accurate representation of intricate electromagnetic field distributions at the micron scale. Equally crucial is the selection of wave sources; plane wave sources need careful alignment of

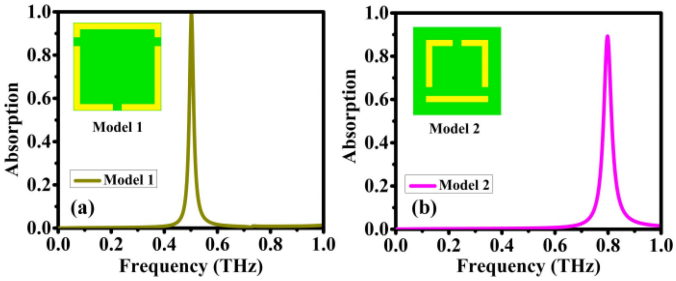

Fig. 2. These are the different absorption properties of the two designs: (a) Models 1; and (b) model 2.

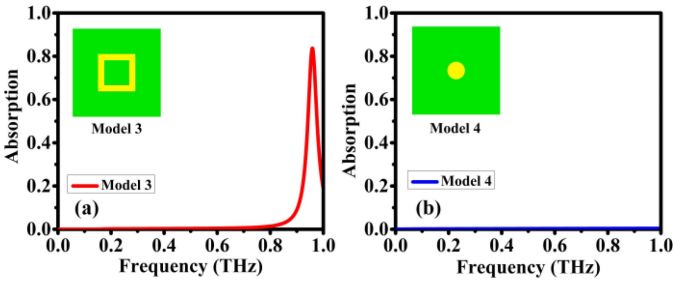

Fig. 3. These are the two designs' various absorption qualities: (a) Model 3; and (b) model 4.

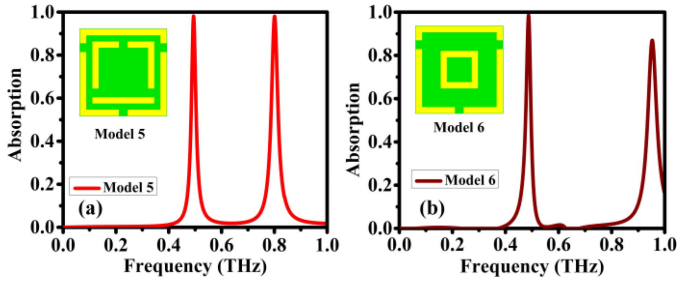

Fig. 4. These are the two designs' distinct absorption characteristics: (a) Model 5; and (b) model 6.

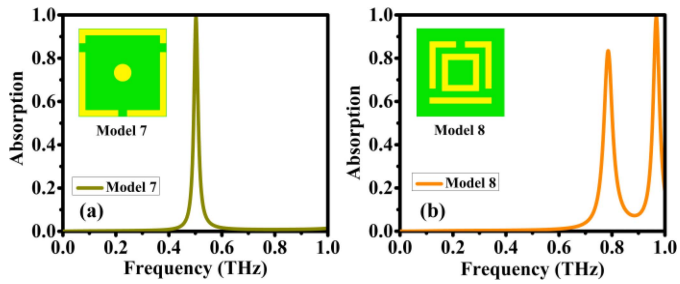

Fig. 5. These are the two designs' distinct absorption characteristics: (a) Model 7; and (b) model 8.

polarization for uniform illumination in THz simulations, while port sources can be used for specific cases. Additional considerations include exploiting symmetry planes, defining accurate material properties, and utilizing post-processing techniques to analyze absorption spectra and electric field distributions for performance evaluation and design optimization. By addressing these factors within CST Studio, effective simulations of micron-scale THz metamaterial absorbers can be conducted, providing valuable insights into absorption properties and potential applications in biosensing.

III. Results and Discussion

Using CST Studio, the sensor was developed and simulated. The expression provided absorption, while the ground plane prevented transmission through the model.

$$A = 1 - R - T = 1 - |S_{11}|^2 - |S_{21}|^2 \tag{4}$$

The S-parameters for reflection and transmission are denoted by S_{11} and S_{21}, respectively. As a result, the reflection coefficient R should be kept as low as possible to achieve maximal absorption. In order to investigate how resonator design affects absorption capacity in the terahertz region, twelve models are displayed in Figs. 2–7. Fig. 2 depict absorption spectra for absorbers composed of Model 1 and Model 2. In these illustrations, the absorber demonstrates narrowband absorption of 99.5% and 89.3% at frequencies of 0.5, and 0.8 THz, respectively. Additionally, the absorption spectrum for Model 3 and Model 4 was simulated, as illustrated in Fig. 3. The outcomes reveal absorption peaks at 0.95 THz is above 80%, while Model 4 show no absorption in range from 0-1 THz. The fact that there are no resonance or interactions in the 0-1 THz range means the model doesn't respond much to those frequencies. But it might have a point where it absorbs information beyond 1 THz, which could be important for higher-frequency spectrum. Even though it doesn't react much in the 0-1 THz range, we keep the model because it's good at dealing with a tasks that involve frequencies higher than 1 THz. It's useful in situations where we need responses to these higher frequencies. So, even though we looked at a specific range, the model stays valuable because it can handle a wide range of tasks beyond the proposed range.

In Fig. 4, the 5th model features two peaks at approximately 0.5 THz and 0.8 THz respectively, signifying absorption exceeding 99% at both frequency spectrums. The 6th model, reveals dual peaks at roughly 0.5 THz and 1 THz. The first peak demonstrates absorption exceeding 99%, while the second peak falls short of complete absorption, registering below 90%, as illustrated in Fig. 4. The 7th model demonstrates the capability to absorb energy in one bands at approximately 0.5 THz as shown Fig. 5. The model 8th configuration exhibited two absorption peaks with a remarkably high concentration, each exceeding 80% and 99% operating at 0.8 and 1 THz respectively.

The absorption spectra in Fig. 6 represent absorbers made from model 9 and model10 respectively. These figures show that the absorber exhibits a high level of absorption, with 85.5% absorption at a frequency of 0.8 THz and 82.8% absorption at a frequency of 1 THz. The 11th model, illustrated in Fig. 7. It displays two absorption peaks around 0.5 THz and 0.8 THz, with the first peak achieving over 99.5% absorption capacity. However, the second peak little falls short of complete absorption as its capacity remains up to 99%. Moving on to the 12th

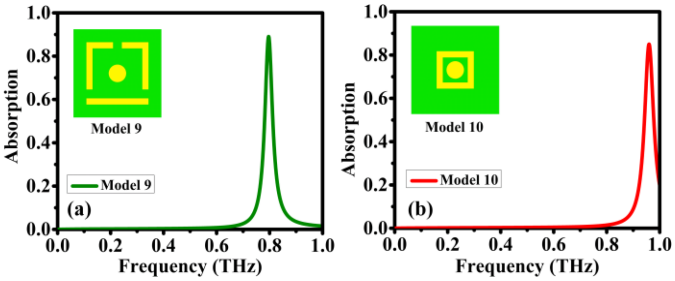

Fig. 6. These are the two designs' distinct absorption characteristics: (a) Model 9; and (b) model 10.

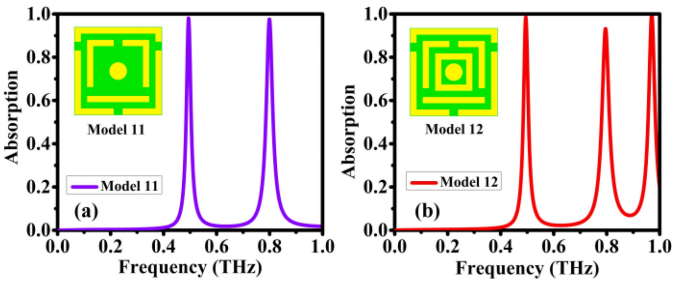

Fig. 7. These are the two designs' distinct absorption characteristics: (a) Model 11; and (b) model 12 (proposed biosensor design).

models, the models exhibit a three absorption peaks at approximately 0.495 THz, 0.796 THz and 0.97 THz with absorption capacities exceeding 99%, 90% and 99% respectively. Fig. 7 visually illustrates these findings. Comprehensive characterization and performance assessments are imperative for a thorough understanding of terahertz (THz) metamaterials functioning as perfect absorbers. These models offer valuable insights into the specific components influencing signal resonance across various THz frequencies. Researchers can enhance design and manufacturing processes by leveraging these insights to achieve essential absorption properties within this frequency range. The recommendation of the 12th model as a biosensor in the 0 to 1 THz range stems from its triple-band design, providing advantages over both single-band and dual-band sensors. While single-band models, like the first and seventh, excel in simplicity during fabrication and measurement, they suffer from limitations in sensitivity to diverse bimolecular interactions. Dual-band sensors, as seen in the fifth and eleventh models, display commendable performance; however, the preference for the triple-band configuration lies in its heightened sensitivity, specificity, and versatility. This triple-band approach enables a more thorough and detailed analysis of terahertz interactions with biological samples, addressing the complexities of bimolecular signatures and minimizing cross-sensitivity, thus establishing it as the preferred choice for advanced bio sensing applications.

Furthermore, the study examined into the absorption characteristics by altering substrate types, namely FR-4, Rogers RT5780, polyethylene terephthalate (PET), ArlonAD430, and ArlonAD410. These materials, such as FR4 and Rogers, are commonly employed as substrate layers in various applications.

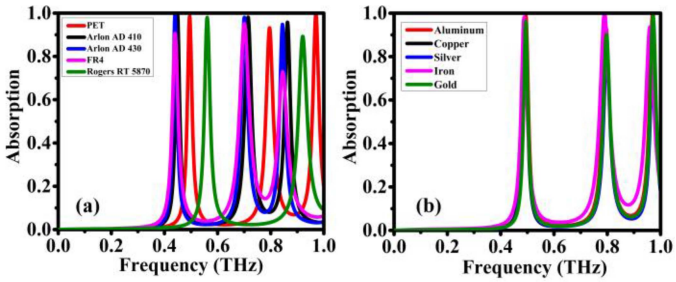

Fig. 8. Absorption spectra for the suggested design under various: (a) Substrate material and (b) resonator material conditions.

However, in certain printed circuit board (PCB) processes, especially in the terahertz frequency band, FR4 and Rogers5870 prove challenging at higher frequencies, FR-4 exhibits increased dielectric losses, dispersion, and absorption of signals. To address this, we opted for the PET dielectric layer as a substrate due to its convenient implementation in the lithographic technique for terahertz frequency spectrums. In examining the dielectric variations and their impact, it became evident that the choice of substrate material significantly influenced the results. The PET dielectric layer's permittivity normally ranges from 3.0 to 3.4. However, the precise values may differ depending on elements like the temperature, frequency of the applied electric field, and the PET material's particular composition. PET is widely regarded as a low-loss dielectric substance. Its low dissipation factor and relatively low dielectric losses make it appropriate for situations where the amount of energy wasted as heat during electrical operations is kept to a minimum. Because of this property, PET may be used in a variety of electronic applications where low dielectric loss is required for effective operation, such as capacitors and insulating layers in electronic devices. Fig. 8(a) illustrates that ArlonAD430 and ArlonAD410 yield identical absorption 99% values for the first peak at 0.4 THz. However, for the second peak, ArlonAD430 exhibited 99% absorption at 0.7 THz, while ArlonAD410 demonstrated higher absorption at approximately 99% at 0.72 THz. Contrastingly, FR4 and Rogers RT5870 exhibited three peaks FR4 material the third band has not reached 80% so the third band is not a perfect absorber and other two absorption peaks with values exceeding 85% at different frequencies. The PET material showcased three peaks resonating at 0.495, 0.796 and 0.97 THz, whereas the Rogers RT5780 material presented two peaks at higher frequencies of 0.5 and 0.9 THz. The materials employed in the study comprised of aluminum, copper, silver, iron, and gold. As depicted in Fig. 8(b), the outcomes indicate a relatively uniform performance among these materials. However, it is noteworthy that iron exhibited favorable outcomes compared to the other materials, marking a departure from the overall trend observed in the experiment. Aluminum, copper, silver, iron, and gold were selected for biosensor resonators and grounds due to their distinct electrical properties. These materials optimize signal transmission, conductivity, and stability, essential for efficient biosensor functionality in detecting and analyzing biological substances with precision and sensitivity.

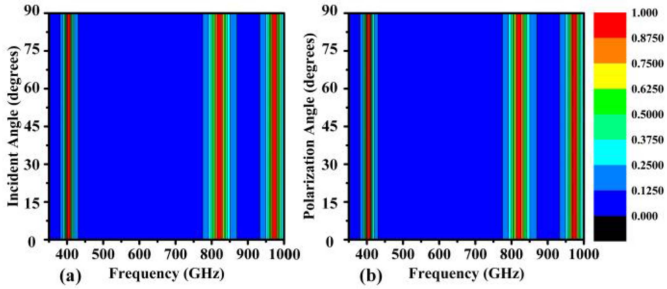

Fig. 9. Impact of angle modification on absorption rate is investigated for: (a) Incidence angle and (b) polarization angle.

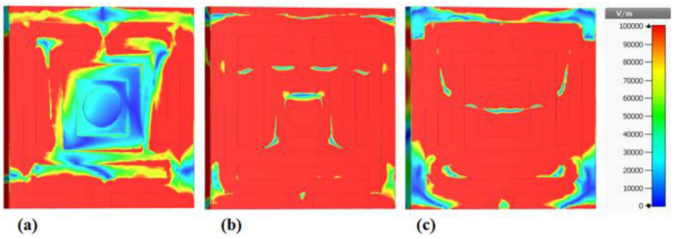

Fig. 10. Distributions of the metamaterial structure field are shown on a colour map: (a) E-field at 0.495 THz, (b) E-field at 0.796 THz, and (c) E-field at 0.97 THz.

In imaging and sensing applications, polarization can lead to suboptimal signal-to-noise ratios (SNR), potentially biasing results. The symmetry of the proposed design ensures that the sensor's polarization independence is maintained [1], [2]. Signal-to-noise ratios (SNR) with polarization and incident angles arises because these angles affect electromagnetic wave transmission efficiency, influencing the quality of received signals by impacting signal strength and noise levels in communication systems. This characteristic is illustrated in Fig. 9, where absorption properties appear largely unaffected despite variations in polarization angles, thereby avoiding any complications. The model considered incidence angles from 0° to 90°, as shown in Fig. 9(a), and observed that the extreme absorption regions remained unchanged for different orientations. Additionally, polarization angles ranging from 0° to 90° were tested, as indicated in Fig. 9(b), revealing consistent behavior of the extreme absorption regions across various angles. This affirms the reliability of the proposed model across a spectrum of incidence angles and polarizations. Signal-to-noise ratios benefit from the stability of both polarization and incident angles. The constancy of these angles enhances signal quality, diminishes noise, and ensures more dependable and precise measurements.

The analysis for E-field distribution was analyzed for three resonating frequencies as shown in Fig. 10. Analyzing E-field distributions in CST Studio for metamaterial perfect absorber design entails a dual strategy. Examining the z-component, Ez, provides insights into localized light-matter interaction, identifying regions of intense field confinement crucial for efficient energy conversion into heat. Scrutinizing Ez variations near specific features aids in understanding resonance behavior. Additionally, analyzing the magnitude of the E-field, |E|, reveals hot spots critical for absorption efficiency. This synergistic analysis empowers comprehensive design optimization, minimizing energy escape and achieving peak terahertz absorption performance. The energy concentration in the outer region is observed in Fig. 10(a) for the 0.495 THz. Fig. 10(b) represents the E-field distribution for the 0.796 THz. The equal energy concentration in the entire region is observed. The E-field response for 0.97 THz is observed in the Fig. 10(c). The outer region concentration is reduced but the center region E-field concentrations remain healthy. The suggested design structure provides a good E-field response for the different resonating frequencies therefore it is useful for biomedical applications. These design steps are helpful for understanding design performance.

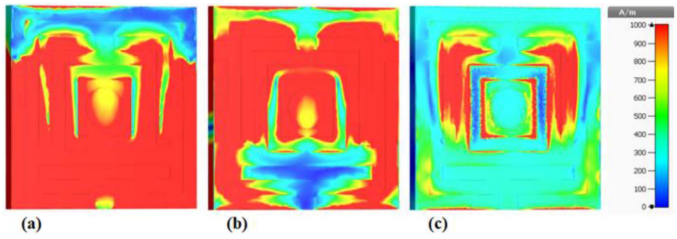

Fig. 11. Illustrated colour map shows the field distributions of the proposed metamaterial structure: (a) H-field at 0.495 THz, (b) H-field at 0.796 THz, and (c) H-field at 0.97 THz.

The distributions of fields offer valuable information about the resonance process and contribute to a better comprehension of design performance. Analyzing the electric and magnetic field intensities at various frequencies makes it clear how particular components influence signal resonances. This assessment and performance analysis is instrumental in optimizing designs for specific resonance frequencies, thereby enhancing the overall performance of biosensors. Additionally, ongoing research includes an examination of magnetic field distribution as another crucial parameter. In CST Studio, both the z-component of the magnetic field (Hz) and the absolute value of the magnetic field (|H|) are viable for determining magnetic field distribution, each catering to distinct analytical needs. Hz provides directional insights into magnetic field flow, aiding in visualizing field patterns and identifying regions of concentration. Conversely, |H| quantifies the magnetic field's magnitude, enabling quantitative analysis and comparison. The choice between Hz and |H| depends on specific analytical objectives, with Hz suitable for visualizing directional characteristics and |H| for quantitative analysis. Utilizing both metrics in conjunction with relevant field components offers a comprehensive understanding of the electromagnetic field distribution. Fig. 11 represents a H-field response for different resonating frequencies. The H-field response for 0.495 THz is shown in Fig. 11(a). The good energy concentration is observed in the majority of regions. H-field concentration for 0.796 THz represents energy concentration focused towards the center region as shown in Fig. 11(b). The H-field is more confined as shown in the Fig. 11(c) for the resonance of 0.97 THz. The high magnetic field overserved for the 0.495 THz, and it represents a good susceptibility to EM wave absorption.

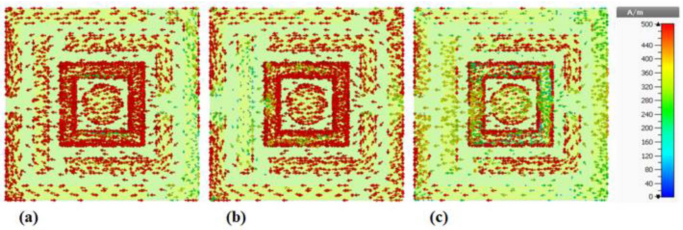

Fig. 12. Surface current distribution of the recommended metamaterial design: (a) At 0.495 THz, (b) at 0.796 THz, and (c) at 0.97 THz.

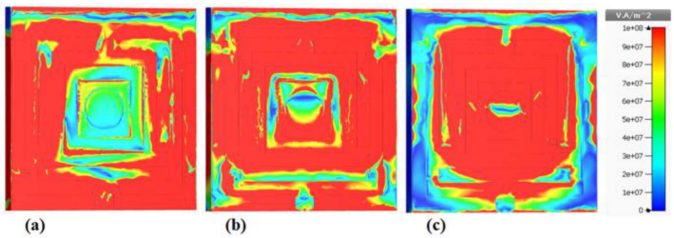

Fig. 13. Examination of the power flow at: (a) At 0.495 THz, (b) at 0.796 THz, and (c) at 0.97 THz.

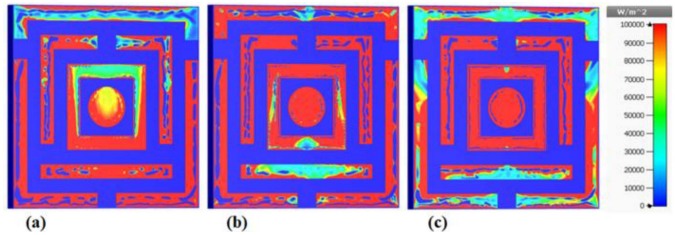

Fig. 14. Examination of the surface power loss at: (a) At 0.495 THz, (b) at 0.796 THz, and (c) at 0.97 THz.

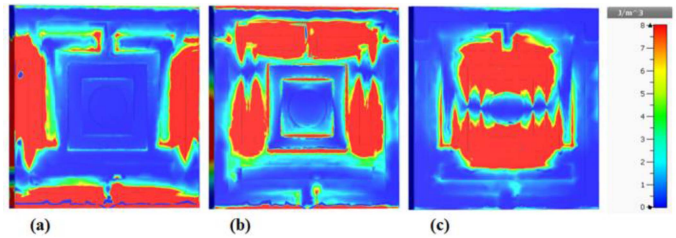

Fig. 15. Examination of the electric energy density at: (a) At 0.495 THz, (b) at 0.796 THz, and (c) at 0.97 THz.

To gain a deeper insight into the physical absorption process of the suggested metamaterial absorbers, the investigation focused on analyzing the distribution of surface currents into the top layer of the proposed design. The circular movement of current represents a good magnetic field response. The magnetic surface charge plot is observed in Fig. 12(a) for the 0.495 THz, and the charge flow is parallel and antiparallel. The antiparallel flow indicates a good magnetic field. The H-field aligned with the magnetic response. Fig. 12(b) shows surface current for 0.796 THz, and H-field concentration is a little bit reduced in the outer region. Fig. 12(c) shows a H-filed for the 0.97 THz. A good concentration of surface charge is observed in the centered region.

The power flow analysis of the proposed design structure is analyzed for different resonances. Fig. 13(a) shows high dense power flow into the outer region of the structure for the 0.495 THz. The power flow is enhanced into the center region for the 0.796 THz as shown into Fig. 13(b). The peak power concentration is observed for the 0.97 THz as shown in Fig. 13(c). The power flow is highly concentrated in the suggested design structure; therefore it represents a good utilization of incoming EM waves.

The surface power loss graph for a biosensor is an important tool for analyzing and refining the device's performance. The response depicts power loss at the sensor's surface and gives insights into the biosensor's energy use. This information helps to fine-tune the sensor's design parameters to reduce power losses and improve overall performance. The graph helps to identify areas for development, which contributes to the optimization of sensitivity and accuracy in biosensor applications. The surface power loss graph for the 0.495 THz is represented in Fig. 14(a). The top and inner region represents a low surface power loss. The surface power loss for 0.796 THz shows power loss area has started moving from the top area to the bottom area as shown into the Fig. 14(b). The analysis of power loss for 0.97 THz is represented in Fig. 14(c). The surface power loss is reduced for the higher resonance.

One way to comprehend the distribution and concentration of electric energy inside the operating components of a biosensor is to look at its electric energy density. To optimize the sensor's performance and design, this study is necessary. Electric energy density helps to improve the sensitivity and efficiency of the sensor. The electric energy density is concentrated on both sides and the bottom of the structure for the 0.495 THz is represented in Fig. 15(a). The 0.796 THz of resonance represents an electric density that moves towards the bottom to top sides and near the center region from the outer sides as shown in Fig. 15(b). Fig. 15(c) shows a more confined and centered concentrated electric energy density for the 0.97 THz.

The examination of magnetic energy density in a biosensor serves the purpose of understanding the distribution and concentration of magnetic energy within the sensor's operational components. This analysis helps to identify regions where magnetic energy is concentrated or dispersed unevenly, providing insights for adjustments to enhance the sensor's sensitivity and efficiency. The magnetic energy density for 0.495 THz of resonance is shown in Fig. 16(a), and it is concentrated towards the bottom side of the structure. The 0.796 THz shows a magnetic field density shift towards an upper side of the structure as shown in Fig. 16(b). Fig. 16(c) shows a highly concentrated magnetic field near the center region for the 0.97 THz.

The Proposed model, three absorption peaks are observed around 0.5 THz, 0.8 THz, and 0.97 THz, each with absorption capacities surpassing 98%, 94%, and 99% respectively. These peaks indicate highly efficient absorption of electromagnetic waves at those frequencies. Additionally, the in-phase response

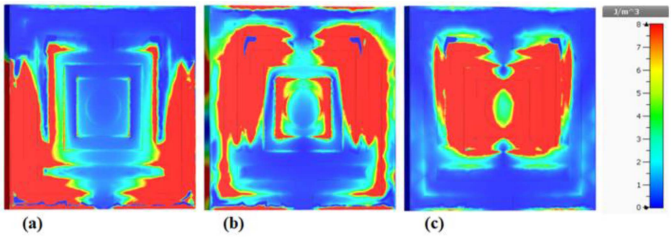

Fig. 16. Examination of the magnetic energy density at: (a) At 0.495 THz, (b) at 0.796 THz, and (c) at 0.97 THz.

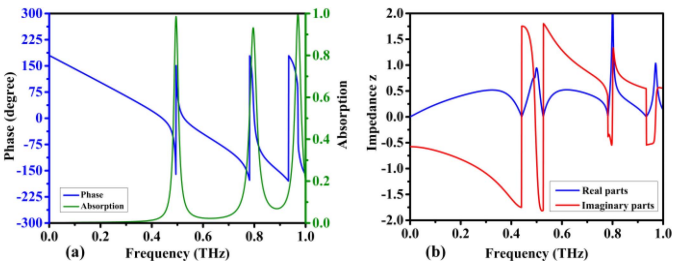

Fig. 17. Simulated responses of parameters of the proposed model. (a) Phase, (b) Impedance z.

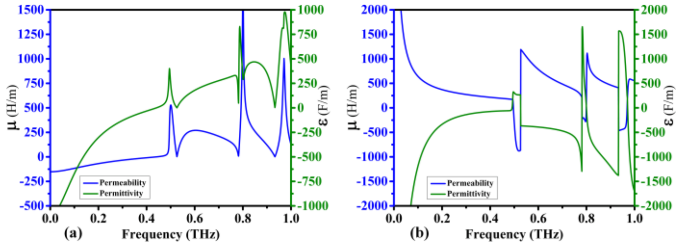

Fig. 18. (a) Real parts of permeability μ and permittivity ε, (b) imaginary parts of permeability μ and permittivity ε of the proposed absorber.

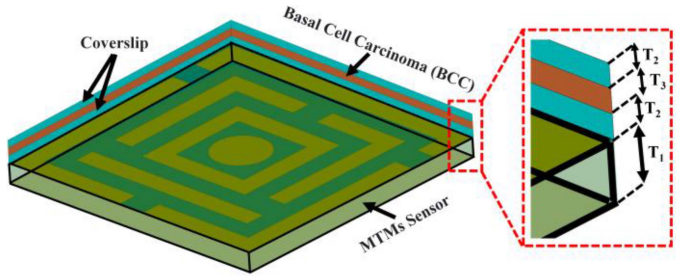

Fig. 19. Suggested biosensor investigates the absorption coefficient in both healthy skin and non-melanoma skin cancer.

within the range of -180^0 to 180^0 degrees suggests that the absorbed energy is effectively converted without significant phase distortion, enhancing the absorber's performance across the resonance frequencies as depicted in Fig. 17(a). The reflection of the incident electromagnetic (EM) wave from the absorber is effectively minimized due to (5), where Z_A represents the impedance of the metamaterial absorber and Z_o is the impedance of free space. The input impedance Z_A of the absorber is determined by the permeability (μ_o) and permittivity (ε_o) constants of free space, along with their respective frequency-dependent relative values (μr and εr). Thus, when Z_A equals Z_o, there is minimal reflection of the EM wave from the absorber, maximizing absorption, as described in (5). This Plot is illustrated in Fig. 17(b).

$$\Gamma_\omega = \frac{Z_A(\omega) - Z_0}{Z_A(\omega) + Z_0} \tag{5}$$

$$Z_A = \sqrt{\frac{\mu_0\,\mu_r(\omega)}{\varepsilon_0\,\mu\varepsilon_r(\omega)}} \tag{6}$$

$$Z_0 = \sqrt{\frac{\mu_0}{\varepsilon_0}} \tag{7}$$

Fig. 18(a) and (b) illustrate the comparison of the real and imaginary components of effective permittivity and permeability, revealing significant changes, particularly near resonance regions, demonstrating shifts in electromagnetic characteristics. Of particular interest is the considerable alteration in the imaginary part of magnetic permeability, aligning with frequencies linked to absorption modes. This observation confirms the prevalent magnetic resonance attributes of the Frequency-Selective Magnetic Metamaterial Absorber (FMMA). Such resonance phenomena underscore FMMA's ability in selectively absorbing electromagnetic waves at specific resonance frequencies. This quality holds promise for various applications in fields such as telecommunications and sensing, where precise control over frequency responses is crucial for optimal device performance and functionality.

IV. Diagnosis of Non-Melanoma Skin Cancer

The Non-Melanoma Skin Cancer Diagnostic Biosensor is a visually appealing tool that uses advanced technology to identify and diagnose non-melanoma skin cancer in its early stages. The ability to accurately predict and analyze signal transmission and absorption using microwave imaging (MWI) enhances the ability to identify cancer cells. This new method overcomes current barriers to quickly and accurately identifying non-melanoma skin cancers, perhaps providing a way to improve early detection and diagnosis. The sensor's proposed detection of non-melanoma skin cancer is shown in Fig. 19. To obtain error-free results, we used two coverslips. As shown in Fig. 19, a skin sample is sandwiched between these two glass coverslips to prepare basal cells. Diagnosis is made using a refractive index of 1.360 for healthy skin and 1.380 for non-melanoma skin cancer, respectively [30], [31], [32], [33], [34], [35].

Fig. 20(a) shows the results of detecting non-melanoma skin cancer and healthy skin. For clean and malignant skin, the results of the first peak between 0.40 THz and 0.55 THz were analyzed. Fig. 20(b) shows that there is a significant difference between clean skin cancer and non-melanoma skin cancer, with a difference equivalent to 0.02683 THz or 26830 MHz. Fig. 21(a) shows the detection results of normal skin and non-melanoma skin cancer. For the second peak, between 0.65 THz and 0.85 THz,

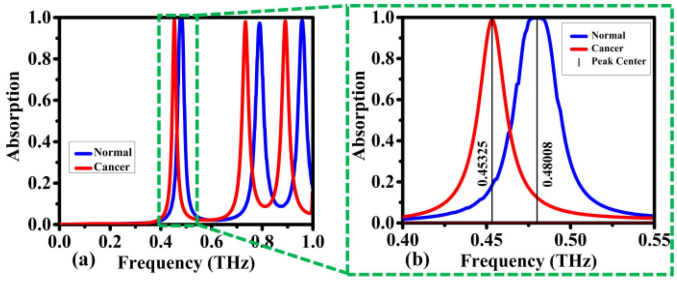

Fig. 20. Proposed biosensor detects the absorption coefficients for normal skin and non-melanoma skin cancer; the frequency range is between: (a) 0–1 THz, (b) 0.4–0.55 THz.

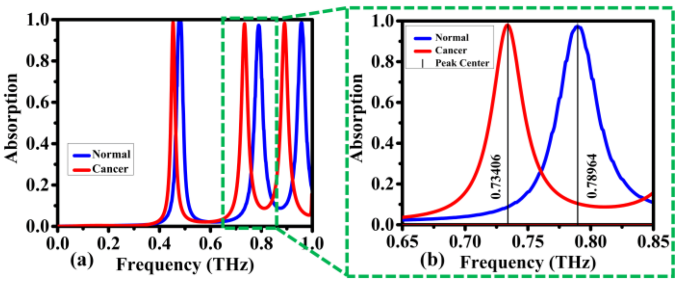

Fig. 21. Proposed biosensor evaluates the absorption coefficients for normal skin and non-melanoma skin cancer; the frequency range is between: (a) 0–1 THz, (b) 0.65–0.85 THz.

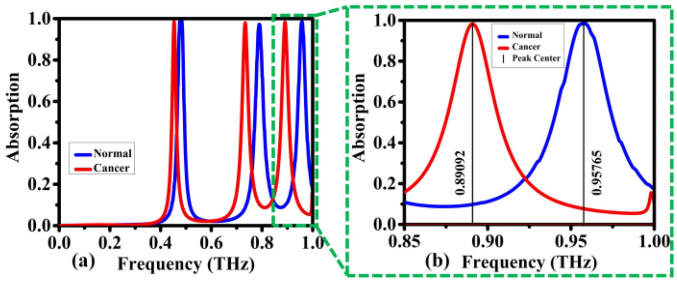

Fig. 22. Proposed biosensor evaluates the absorption coefficients for normal skin and non-melanoma skin cancer; the frequency range is between: (a) 0–1 THz, (b) 0.85–1 THz.

the results related to healthy and malignant skin were compared. The data, shown in Fig. 21(b), shows that there is a significant difference between healthy skin and non-melanoma skin cancer, with the difference corresponding to 0.05558 THz or 55580 MHz. Fig. 22(a) also shows the detection results for healthy skin and non-melanoma skin cancer. For clean and malignant skin, the results of the third peak between 0.85 THz and 1 THz were analyzed. There is a significant difference between clean skin and non-melanoma skin cancer, as shown in Fig. 22(b), with a difference of 0.06673 THz, equivalent to 66730 MHz.

The quality factor (Q factor) and Figure of Merit (FOM) are important metrics to evaluate the effectiveness of triple-band perfect absorber metamaterials as sensors. By dividing one performance metric, such as sensitivity, by another metric, such as bandwidth or noise level, FOM determines the effectiveness of the sensor. The resonance quality in the system is evaluated

TABLE II
BIO-SENSING PERFORMANCE COMPARISONS OF VARIOUS SENSOR APPLICATIONS BASED ON THZ METAMATERIAL

Ref.	Q	S (THz/RIU)	FOM (RIU−1)	Bio-application	Year Published
[38]	5.58	0.02432	0.1216	detection of Penicillia	2014
[41]	-	0.0242, 0.02438	-	detection of Virus	2017
[42]	6.6	0.285	1.88	sensor	2020
[43]	-	0. 960	-	Biosensor, Collagen	2020
[44]	-	0. 2833	-	Polystyrene particle	2021
[39]	2.43	1.21	2.75	Cancer Diagnostics, Biosensor	2022
[45]	8.21, 6.05	0. 203	1.81, 1.57	sensor	2022
[40]	-	1.06	0.166	detection of avian influenza virus	2022
This work	23.3, 24.1, 33.97	1.342, 2.78, 3.337	63.11, 84.134, 116.85	Non-Melanoma Skin Cancer Diagnostics	-

by the dimensionless Q factor. High values of the FOM and Q coefficients mean improved performance, so they are important for evaluating the effectiveness of triple-band perfect absorber metamaterials in sensing-related applications. The ability of perfect metamaterial absorbers to respond to changes in the refractive index of the surrounding medium determines their sensitivity. The resonance frequency or absorption peak shift of the absorber is used to evaluate this sensitivity. The increased sensitivity indicates the ability to identify and differentiate small variations in refractive index, making it suitable for uses such as identifying early-stage cancer. When there is not significant variation in refractive index, sensitivity plays an important role in obtaining accurate results.

A sensor's figure of merit (FOM), quality factor (Q-factor), and sensitivity (S) are three of its most important performance parameters. A sensor's selectivity is expressed by its full output measurement figure of merit (FOM), which is equal to the normalization of the sensitivity to the full width at half maximum (FWHM) of the resonant dip. Our manuscript extensively compares our biosensor's performance with existing literature, focusing on figures of merit (FOM), quality factors (Q-factor), and sensitivity. Equations (8), (9), and (10) determine sensitivity, crucial for performance evaluation. A detailed comparison in Table II showcases differences in sensitivity and other key parameters, aiding in understanding our biosensor's efficacy.

$$FOM = \frac{S}{FWHM} \tag{8}$$

The Q_{factor}, which has a formula, is used to assess the sharpness of the resonance.

$$Q_{factor} = \frac{\lambda}{FWHM} \tag{9}$$

TABLE III
COMPARISON BETWEEN THE STUDY ON PERFECT METAMATERIALS IN THE TERAHERTZ BAND AND THE SUGGESTED BIOSENSOR

References	Frequency operating THz	Techniques used	Material substrate	Absorptivity	Application
[46]	0-3	PET/FSS/UV glue/ Graphene	PET	0.99, 0.80, 0.95	Multifunctional Tunable Terahertz
[47]	7-9.5	Au/SiO2/ Graphene	SiO2	0.98	Multi-Frequency Broadband and Ultra-Broadband
[48]	1−2.2	Au/dielectric Teflon/Au	dielectric Teflon	0.99	Sensor
[49]	0.7-5	Ion gel/Graphene/Teflon/Gold	Teflon	>0.96	polarization-sensitive
[50]	0.5−4.5	graphene/Topas//Au	Topas spacer	0.99, 0.98, 0.99	Ultra-Broadband Absorber
[51]	1−3	bulk Dirac semimetal/photonic crystal/Au	photonic crystal plate	0.97, 0.98, 0.99	Narrowband perfect absorber
[52]	1.5-1.7	Gold/silicon dioxide/ Gold	silicon dioxide	0.972, 0.991	biosensor for detecting coronaviruses
[53]	0-0.37	Glass/InSb/MgF2/InSb	Glass	0.998	Colon Cancer Detection
[39]	0.5-2.5	SiO2/Graphene	SiO2	-	Breast cancer detection
[54]	1−3	Au/dielectric layer/Au	dielectric layer	0.99, 0.99	Sensor
[55]	2−6	graphene/Au/SiO2/Au	SiO2	0.99	Refractive index sensor
This work	0−1	Al/PET/Al	PET	0.983, 0.94, 0.9999	Biosensor, Non-Melanoma Skin Cancer Diagnostics and Microwave Imaging

wavelength of resonance, represented as λ. Metamaterial-oriented the sensitivity of terahertz (THz) detection is greatly enhanced by terahertz (THz) biosensor. Two interpretations of sensitivity are frequently used in scientific literature. Frequency sensitivity is the first.

$$S = \frac{\Delta f}{\Delta n} \tag{10}$$

where n represents the change in refractive index (RI), often written in terms of refractive index units (RIU), and Δf is the frequency shift of the resonance peak. Another method is to calculate S = ΔI/Δn, the intensity frequency, where ΔI is the fluctuation of the resonance intensity [36], [37].

Previous studies have demonstrated the potential of metamaterial-based biosensors across various applications. For instance, one study showcased a penicillin detection biosensor with a Figure of Merit (FOM) of 0.1216 RIU^{-1}, a quality factor of 5.58, and sensitivity (S) of 0.02432 THz/RIU [38]. Another developed a biosensor for breast cancer detection with a Q-factor of 2.43, FOM of 2.75 RIU^{-1}, and 1.21 THz/RIU sensitivity [39]. Additionally, a third study reported a biosensor for avian influenza virus with S = 1.06 THz/RIU and FOM = 0.166 RIU^{-1}, lacking a Q-factor value [40]. In contrast, our proposed biosensor for non-melanoma skin cancer diagnosis introduces a novel design featuring three distinct resonance bands: Band 1 with a Q-factor of 23.3, FOM of 63.11 RIU^{-1}, and S of 1.342 THz/RIU; Band 2 with a Q-factor of 24.1, FOM of 84.134 RIU^{-1}, and S of 2.78 THz/RIU; and Band 3 with a Q-factor of 33.97, FOM of 116.85 RIU^{-1}, and S of 3.337 THz/RIU (as presented in Table II). Notably, our design exhibits significantly higher FOMs across all bands compared to previous biosensors, indicating potentially superior performance in distinguishing healthy skin from newly infected non-melanoma skin cancer.

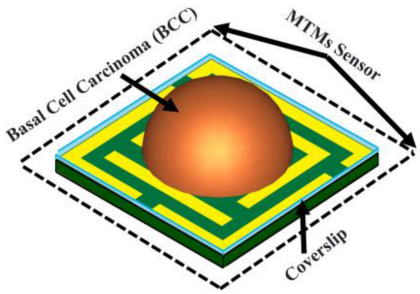

Fig. 23. Diagnosis of non-melanoma skin cancer using the MWI approach.

This suggests our proposed biosensor ensures conclusive results in such differentiation. The Q-factor, FOM, and sensitivity play crucial roles in assessing biosensor performance, where higher values signify better detection capabilities and accuracy.

Based on the physical quality assessment for biosensing of previously developed biosensors, especially for biological applications, our results may open new directions. for relevant applications in non-melanoma skin cancer research, as explained in Table III. Using terahertz imaging, this significant frequency difference facilitates the diagnosis of non-melanoma skin cancer. Healthcare providers can reliably identify and diagnose non-melanoma skin cancer, allowing for early intervention and treatment by analyzing the skin's terahertz frequency spectrum of the patient. The proposed PET substrate based simple design helps for the cost reduction, and easy to fabricate compared to the other techniques as well it represents a good absorption rate compared to other designs.

The findings were corroborated with microwave imaging techniques based on the fundamentals of image reconstruction in the terahertz band. As illustrated in Fig. 23, a skin sample

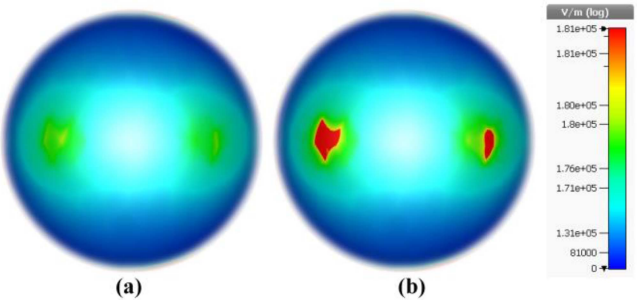

Fig. 24. E-field MWI technique results at 0.495 THz: (a) Healthy skin, (b) non-melanoma skin cancer.

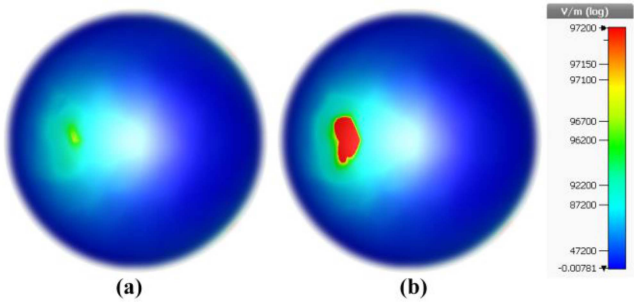

Fig. 25. E-field MWI technique results at 0.796 THz: (a) Healthy skin, (b) non-melanoma skin cancer.

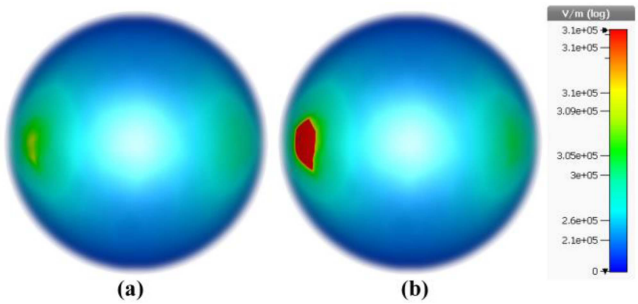

Fig. 26. E-field MWI technique results at 0.97 THz: (a) Healthy skin, (b) non-melanoma skin cancer.

was deposited on a coverslip to be tested using the suggested biosensor. Terahertz E-field imaging utilizing a triple-band, micron-sized metamaterial perfect absorber biosensor presents a promising avenue for non-invasive skin cancer detection. The observed high E-field intensity hotspots (red areas) corresponding to non-melanoma skin cancer likely stem from distinct dielectric properties of tissues and enhanced resonant interactions at specific terahertz frequencies, as shown in Fig. 24(a). This notable contrast in E-field intensity compared to healthy skin regions (another color areas), as shown in Fig. 24(b), indicates a potential early-stage cancer diagnostic capability, meriting further research and validation for robust clinical translation and enhanced skin cancer detection outcomes. The presence of red areas in the terahertz image signifies the potential presence of non-melanoma skin cancer, as healthy skin and cancerous tissue exhibit disparate dielectric properties affecting their interaction with terahertz waves. In the terahertz range, the unique vibrational resonances of molecules within tissue, such as water and proteins, further contribute to differential dielectric properties, influencing terahertz wave propagation and scattering. The distinctive types and distributions of these molecules in non-melanoma skin cancer result in observable changes in terahertz wave interactions, manifested as hotspots (red areas) in the imaging. This integrated understanding of terahertz E-field imaging, dielectric properties, and molecular resonances provides a comprehensive framework for interpreting observed hotspots in the context of skin cancer detection, highlighting the potential significance of this technology in advancing non-invasive diagnostic methodologies.

As shown in Fig. 25, it illustrates a second-peak terahertz E-field intensity distribution obtained through microwave imaging of healthy skin, as shown in Fig. 25(a), and non-melanoma skin cancer, as shown in Fig. 25(b), using a biosensor. Red areas in the image, denoting high E-field intensity, precisely align with the location of non-melanoma skin cancer while other color areas represent low E-field intensity over healthy skin. This observed contrast in E-field intensity between healthy and cancerous tissue stems from distinct dielectric properties influenced by variations in tissue composition and molecular distributions. The triple-band metamaterial perfect absorber is strategically designed to resonate efficiently at specific terahertz frequencies, including the second peak featured in the figure. These resonances amplify the interaction between terahertz waves and tissue, particularly at the specified frequency, leading to localized hotspots of high E-field intensity within cancerous tissue. The significantly higher E-field intensity observed in the red areas over non-melanoma skin cancer compared to the blue areas over healthy skin suggests potential non-invasive differentiation based on dielectric interactions with terahertz waves. In conclusion, the terahertz imaging technique utilizing a metamaterial-based biosensor exhibits potential for non-invasive early detection of non-melanoma skin cancer, with the observed differential E-field intensity distribution at the second peak frequency representing a promising avenue for further development as a valuable tool for accurate and early cancer diagnosis.

The terahertz E-field image for the third peak reveals intriguing yet nuanced potential for non-melanoma skin cancer detection. While localized high-intensity (red) areas coincide with the cancer lesion, as shown in Fig. 26(b), the overall contrast with healthy skin (another color), as shown in Fig. 26(a), appears less pronounced compared to the first and second peaks. This suggests a weaker resonant enhancement effect at this frequency, potentially limiting the reliability of solely using the third peak for cancer differentiation. While further research and optimization are needed to exploit the full potential of this approach, combining information from all three peaks or exploring other imaging parameters might hold promise for robust and accurate early-stage skin cancer detection.

The investigation into magnetic fields for terahertz imaging has yielded significant potential for non-invasive skin cancer

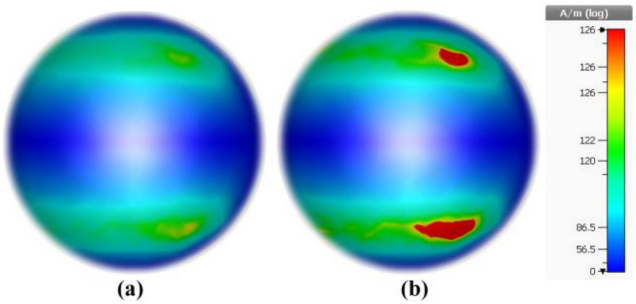

Fig. 27. H-field MWI technique results at 0.796 THz: (a) Healthy skin, (b) non-melanoma skin cancer.

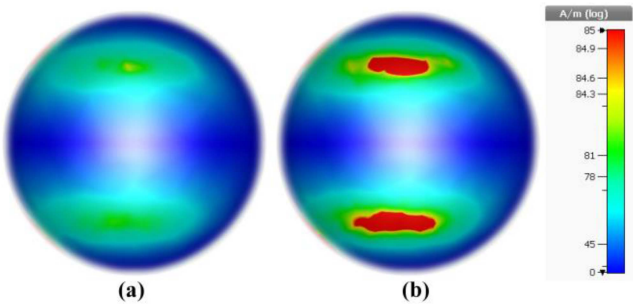

Fig. 28. H-field MWI technique results at 0.97 THz: (a) Healthy skin, (b) non-melanoma skin cancer.

detection, particularly in the context of the second-peak terahertz H-field image obtained through microwave imaging using a biosensor. In this image (Fig. 27), red areas indicating high H-field intensity precisely align with the location of the non-melanoma skin cancer lesion, as shown in Fig. 27(b), creating a distinct contrast with the surrounding healthy skin, as shown in Fig. 27(a). This contrast holds promise for early-stage cancer diagnosis, with key factors contributing to the observed differentiation. Differential magnetic properties, influenced by variations in the magnetic susceptibility of healthy and cancerous tissues due to their cellular composition and molecular distributions, play a pivotal role in terahertz wave interactions. The biosensor's resonant enhancement at specific frequencies, including the second peak, modulates the local magnetic field, potentially amplifying it within cancerous tissue. This resonance-driven enhancement, combined with localized interactions between the enhanced magnetic field and specific biomolecules within the cancer lesion, may result in observed hotspots of high H-field intensity. The implications of these findings underscore the potential of magnetic fields in terahertz imaging for advancing non-invasive skin cancer detection, highlighting avenues for further research and clinical validation.

Subsequent inquiry focused on the third peak, elucidated in Fig. 28, revealing discernible patterns in magnetic density associated with healthy skin and nonmelanoma skin cancer. Fig. 28(a) illustrates regions characterized by low magnetic density corresponding to healthy skin, while Fig. 28(b) delineates areas of elevated magnetic field density indicative of nonmelanoma skin cancer.

V. Future Perspective

Designing higher sensitivity biosensors for early cancer detection e.g., Early-stage diagnosis of colon cancer, adrenal gland cancer (PC-12), breast cancer, cervical cancer (HeLa), and blood cancer using terahertz (THz) electromagnetic (EM) wave imaging bio-sensors.

VI. Conclusion

This paper introduces an innovative microscale biosensor designed to operate in the THz range, aiming for high sensitivity and efficient diagnostics of non-melanoma skin cancer (NMSC). The fundamental structure of the biosensor features metamaterial cells tailored to exhibit specific absorption properties, particularly absorption peaks positioned at distinct frequencies within the low-THz range (0.1 to 1.0 THz). These characteristics play a crucial role in enabling the device to distinguish between normal skin and skin affected by non-melanoma cancer. The interaction between the skin and THz waves, encompassing wave propagation and scattering, is influenced by the dielectric properties, which differ between healthy and cancerous tissues. Additionally, the unique vibrational resonances of molecules within the tissue, such as proteins, also impact this interaction. The paper conducts extensive numerical studies to showcase the suitability of the proposed biosensor for diagnosing NMSC. Specific case studies involving healthy and cancerous skin demonstrate the effectiveness of the device. Furthermore, the proposed biosensor is compared to several recently reported THz-range devices, revealing superior overall properties and versatility compared to established benchmarks. These findings open avenues for the further development of non-invasive microwave-imaging-based techniques for detecting NMSC and other types of skin cancer.

References

[1] M. Ciążyńska et al., "The incidence and clinical analysis of non-melanoma skin cancer," *Sci. Rep.*, vol. 11, no. 1, Feb. 2021, Art. no. 4337.
[2] M. J. Eide et al., "Identification of patients with nonmelanoma skin cancer using health maintenance organization claims data," *Amer. J. Epidemiol.*, vol. 171, no. 1, pp. 123–128, Jan. 2010.
[3] E. B. Souto et al., "Non-melanoma skin cancers: Physio-pathology and role of lipid delivery systems in new chemotherapeutic treatments," *Neoplasia*, vol. 30, Aug. 2022, Art. no. 100810.
[4] M. Ciążyńska et al., "Clinical and epidemiological analysis of basosquamous carcinoma: Results of the multicenter study," *Sci. Rep.*, vol. 10, no. 1, Oct. 2020, Art. no. 18475.
[5] J. P. Malone, F. G. Fedok, D. A. Belchis, and M. E. Maloney, "Basal cell carcinoma metastatic to the parotid: Report of a new case and review of the literature," *Ear, Nose Throat J.*, vol. 79, no. 7, pp. 511–519, 2000.
[6] B. S. Cherpelis, C. Marcusen, and P. G. Lang, "Prognostic factors for metastasis in squamous cell carcinoma of the skin," *Dermatologic Surg.*, vol. 28, no. 3, pp. 268–273, Mar. 2002.
[7] V. Samarasinghe and V. Madan, "Nonmelanoma skin cancer," *J. Cutan. Aesthetic Surg.*, vol. 5, no. 1, pp. 3–10, Jan. 2012.
[8] D. Altamura et al., "Dermatoscopy of basal cell carcinoma: Morphologic variability of global and local features and accuracy of diagnosis," *J. Amer. Acad. Dermatol.*, vol. 62, no. 1, pp. 67–75, Jan. 2010.
[9] R. Kumar, M. Kumar, J. S. Chohan, and S. Kumar, "Overview on metamaterial: History, types and applications," *Mater. Today: Proc.*, vol. 56, pp. 3016–3024, Jan. 2022.
[10] S. E. Mendhe and Y. P. Kosta, "Metamaterial properties and applications," *Int. J. Inf. Technol. Knowl. Manage.*, vol. 4, no. 1, pp. 85–89, 2011.

[11] A. F. Almutairi, M. S. Islam, M. Samsuzzaman, M. T. Islam, N. Misran, and M. T. Islam, "A complementary split ring resonator based metamaterial with effective medium ratio for C-band microwave applications," *Results Phys.*, vol. 15, 2019, Art. no. 102675.

[12] M. Z. Mahmud, M. T. Islam, N. Misran, S. Kibria, and M. Samsuzzaman, "Microwave imaging for breast tumor detection using uniplanar AMC based CPW-fed microstrip antenna," *IEEE Access*, vol. 6, pp. 44763–44775, 2018.

[13] N. Misran, S. H. Yusop, M. T. Islam, and M. Y. Ismail, "Analysis of parameterization substrate thickness and permittivity for concentric split ring square reflectarray element," *J. Eng.*, vol. 23, pp. 11–16, 2012.

[14] A. Rahman, M. T. Islam, M. J. Singh, S. Kibria, and M. Akhtaruzzaman, "Electromagnetic performances analysis of an ultra-wideband and flexible material antenna in microwave breast imaging: To implement a wearable medical bra," *Sci. Rep.*, vol. 6, no. 1, 2016, Art. no. 38906.

[15] M. Rokunuzzaman, M. Samsuzzaman, and M. T. Islam, "Unidirectional wideband 3-D antenna for human head-imaging application," *IEEE Antennas Wireless Propag. Lett.*, vol. 16, pp. 169–172, 2017.

[16] J. Cheng, F. Fan, and S. Chang, "Recent progress on graphene-functionalized metasurfaces for tunable phase and polarization control," *Nanomaterials*, vol. 9, no. 3, p. 398, Mar. 2019.

[17] S. Xiao, T. Wang, T. Liu, C. Zhou, X. Jiang, and J. Zhang, "Active metamaterials and metadevices: A review," *J. Phys. D: Appl. Phys.*, vol. 53, no. 50, 2020, Art. no. 503002.

[18] D. Yan et al., "A review: The functional materials-assisted terahertz metamaterial absorbers and polarization converters," *Photonics*, vol. 9, no. 5, 2022, Art. no. 335.

[19] J. Hao, J. Wang, X. Liu, W. J. Padilla, L. Zhou, and M. Qiu, "High performance optical absorber based on a plasmonic metamaterial," *Appl. Phys. Lett.*, vol. 96, no. 25, 2010, Art. no. 251104.

[20] H. Zhang, Y. Cheng, and F. Chen, "Quad-band plasmonic perfect absorber using all-metal nanostructure metasurface for refractive index sensing," *Optik*, vol. 229, 2021, Art. no. 166300.

[21] Z. Ju et al., "Ultra-broadband high-efficiency airy optical beams generated with all-silicon metasurfaces," *Adv. Opt. Mater.*, vol. 9, no. 1, 2021, Art. no. 2001284.

[22] V. Naresh and N. Lee, "A review on biosensors and recent development of nanostructured materials-enabled biosensors," *Sensors*, vol. 21, no. 4, Feb. 2021, Art. no. 1109.

[23] S. Gao et al., "Design of surface plasmon resonance-based D-type double open-loop channels PCF for temperature sensing," *Sensors*, vol. 23, no. 17, 2023, Art. no. 7569.

[24] R. Cheng, L. Xu, X. Yu, L. Zou, Y. Shen, and X. Deng, "High-sensitivity biosensor for identification of protein based on terahertz Fano resonance metasurfaces," *Opt. Commun.*, vol. 473, Oct. 2020, Art. no. 125850.

[25] Y. Cheng and J. Zhao, "Simple design of a six-band terahertz perfect metasurface absorber based on a single resonator structure," *Physica Scripta*, vol. 97, no. 9, 2022, Art. no. 095508.

[26] Z. Huang et al., "High-resolution metalens imaging polarimetry," *Nano Lett.*, vol. 23, no. 23, pp. 10991–10997, 2023.

[27] Z. Geng, X. Zhang, Z. Fan, X. Lv, and H. Chen, "A route to terahertz metamaterial biosensor integrated with microfluidics for liver cancer biomarker testing in early stage," *Sci. Rep.*, vol. 7, no. 1, 2017, Art. no. 16378.

[28] C. Rong, B. Cai, Y. Cheng, F. Chen, H. Luo, and X. Li, "Dual-band terahertz chiral metasurface absorber with enhanced circular dichroism based on temperature-tunable InSb for sensing applications," *Phys. Chem. Chem. Phys.*, vol. 26, no. 6, pp. 5579–5588, 2024, doi: 10.1039/D3CP05528K.

[29] Z. Li, Y. Cheng, H. Luo, F. Chen, and X. Li, "Dual-band tunable terahertz perfect absorber based on all-dielectric InSb resonator structure for sensing application," *J. Alloys Compounds*, vol. 925, 2022, Art. no. 166617.

[30] K. Ahmed, B. K. Paul, F. Ahmed, M. A. Jabin, and M. S. Uddin, "Numerical demonstration of triangular shaped photonic crystal fibre-based biosensor in the Terahertz range," *Inst. Eng. Technol. Optoelectron.*, vol. 15, no. 1, pp. 1–7, 2021.

[31] M. A. Jabin et al., "Surface plasmon resonance based titanium coated biosensor for cancer cell detection," *IEEE Photon. J.*, vol. 11, no. 4, Aug. 2019, Art. no. 3700110.

[32] P. Kumar, V. Kumar, and J. S. Roy, "Dodecagonal photonic crystal fibers with negative dispersion and low confinement loss," *Optik*, vol. 144, pp. 363–369, 2017.

[33] T. Parvin, K. Ahmed, A. M. Alatwi, and A. N. Z. Rashed, "Differential optical absorption spectroscopy-based refractive index sensor for cancer cell detection," *Opt. Rev.*, vol. 28, pp. 134–143, 2021.

[34] P. Sharma, P. Sharan, and P. Deshmukh, "A photonic crystal sensor for analysis and detection of cancer cells," in *Proc. Int. Conf. Pervasive Comput.*, 2015, pp. 1–5.

[35] M. N. Hamza and M. T. Islam, "Designing an extremely tiny dual-band biosensor based on MTMs in the terahertz region as a perfect absorber for non-melanoma skin cancer diagnostics," *IEEE Access*, vol. 11, pp. 136770–136781, 2023.

[36] M. Gómez-Castaño, J. L. Garcia-Pomar, L. A. Pérez, S. Shanmugathasan, S. Ravaine, and A. Mihi, "Electrodeposited negative index metamaterials with visible and near infrared response," *Adv. Opt. Mater.*, vol. 8, no. 19, 2020, Art. no. 2000865.

[37] R. Krause et al., "Ultrafast charge separation in bilayer WS_2/graphene heterostructure revealed by time-and angle-resolved photoemission spectroscopy," *Front. Phys.*, vol. 9, 2021, Art. no. 668149.

[38] S. Park et al., "Detection of microorganisms using terahertz metamaterials," *Sci. Rep.*, vol. 4, no. 1, 2014, Art. no. 4988.

[39] C. Tan et al., "Cancer diagnosis using terahertz-graphene-metasurface-based biosensor with dual-resonance response," *Nanomaterials*, vol. 12, no. 21, 2022, Art. no. 3889.

[40] E. Hoseini, A. Mir, and A. Farmani, "Modeling and proposal of a black phosphorus-based nanostructure for detection of avian influenza virus in infrared region," *Opt. Quantum Electron.*, vol. 54, no. 10, 2022, Art. no. 609.

[41] S. Park, S. Cha, G. Shin, and Y. Ahn, "Sensing viruses using terahertz nano-gap metamaterials," *Biomed. Opt. Exp.*, vol. 8, no. 8, pp. 3551–3558, 2017.

[42] T. Chen, D. Zhang, F. Huang, Z. Li, and F. Hu, "Design of a terahertz metamaterial sensor based on split ring resonator nested square ring resonator," *Mater. Res. Exp.*, vol. 7, no. 9, 2020, Art. no. 095802.

[43] S. Asgari, N. Granpayeh, and T. Fabritius, "Controllable terahertz cross-shaped three-dimensional graphene intrinsically chiral metastructure and its biosensing application," *Opt. Commun.*, vol. 474, 2020, Art. no. 126080.

[44] J. Yang and Y.-S. Lin, "Design of tunable terahertz metamaterial sensor with single-and dual-resonance characteristic," *Nanomaterials*, vol. 11, no. 9, 2021, Art. no. 2212.

[45] H. Hu, B. Qi, Y. Zhao, X. Zhang, Y. Wang, and X. Huang, "A graphene-based THz metasurface sensor with air-spaced structure," *Front. Phys.*, vol. 10, 2022, Art. no. 990126.

[46] S. Zhuang et al., "Graphene-based absorption–Transmission multi-functional tunable THz metamaterials," *Micromachines*, vol. 13, no. 8, 2022, Art. no. 1239.

[47] Z. Chen et al., "Graphene multi-frequency broadband and ultra-broadband terahertz absorber based on surface plasmon resonance," *Electronics*, vol. 12, no. 12, 2023, Art. no. 2655.

[48] A. S. Saadeldin, M. F. O. Hameed, E. M. Elkaramany, and S. S. A. Obayya, "Highly sensitive terahertz metamaterial sensor," *IEEE Sensors J.*, vol. 19, no. 18, pp. 7993–7999, Sep. 2019.

[49] S. Asgari and T. Fabritius, "Numerical simulation and equivalent circuit model of multi-band terahertz absorber composed of double-sided graphene comb resonator array," *IEEE Access*, vol. 11, pp. 36052–36063, 2023.

[50] L. Liu, W. Liu, and Z. Song, "Ultra-broadband terahertz absorber based on a multilayer graphene metamaterial," *J. Appl. Phys.*, vol. 128, no. 9, 2020, Art. no. 093104.

[51] Y. Wang et al., "Terahertz tunable three band narrowband perfect absorber based on Dirac semimetal," *Physica E: Low-Dimensional Syst. Nanostructures*, vol. 131, 2021, Art. no. 114750.

[52] Z. El-Wasif, T. Ismail, and O. Hamdy, "Design and optimization of highly sensitive multi-band terahertz metamaterial biosensor for coronaviruses detection," *Opt. Quantum Electron.*, vol. 55, no. 7, 2023, Art. no. 604.

[53] Z. Vafapour, W. Troy, and A. Rashidi, "Colon cancer detection by designing and analytical evaluation of a water-based THz metamaterial perfect absorber," *IEEE Sensors J.*, vol. 21, no. 17, pp. 19307–19313, Sep. 2021.

[54] B.-X. Wang, Y. He, P. Lou, and W. Xing, "Design of a dual-band terahertz metamaterial absorber using two identical square patches for sensing application," *Nanoscale Adv.*, vol. 2, no. 2, pp. 763–769, 2020.

[55] M.-R. Nickpay, M. Danaie, and A. Shahzadi, "Highly sensitive THz refractive index sensor based on folded split-ring metamaterial graphene resonators," *Plasmonics*, vol. 17, pp. 237–248, 2022.